The Astrophysical Journal, 920:150 (10pp), 2021 October 20 https://doi.org/10.3847/1538-4357/ac1a13

The Impact of Powerful Jets on the Far-infrared Emission of an Extreme Radio Quasar at $z \sim 6$

Sofía Rojas-Ruiz[1,8], Eduardo Bañados[1], Marcel Neeleman[1], Thomas Connor[2,9], Anna-Christina Eilers[3,10], Bram P. Venemans[4], Yana Khusanova[1], Chris Carilli[5], Chiara Mazzucchelli[6,11], Roberto Decarli[7], Emmanuel Momjian[5], and Mladen Novak[1]

[1] Max-Planck-Institut für Astronomie, Königstuhl 17, D-69117, Heidelberg, Germany; rojas@mpia.de
[2] Jet Propulsion Laboratory, California Institute of Technology, 4800 Oak Grove Drive, Pasadena, CA 91109, USA
[3] MIT Kavli Institute for Astrophysics and Space Research, 77 Massachusetts Ave., Cambridge, MA 02139, USA
[4] Leiden Observatory, Leiden University, P.O. Box 9513, 2300 RA, Leiden, The Netherlands
[5] National Radio Astronomy Observatory, P.O. Box O, Socorro, NM 87801, USA
[6] European Southern Observatory, Alonso de Cordova 3107, Vitacura, Region Metropolitana, Chile
[7] INAF—Osservatorio di Astrofisica e Scienza dello Spazio di Bologna, via Gobetti 93/3, I-40129, Bologna, Italy
Received 2021 May 4; revised 2021 July 12; accepted 2021 August 1; published 2021 October 25

Abstract

The interactions between radio jets and the interstellar medium play a defining role for the coevolution of central supermassive black holes and their host galaxies, but observational constraints on these feedback processes are still very limited at redshifts $z > 2$. We investigate the radio-loud quasar PSO J352.4034–15.3373 at $z \sim 6$ at the edge of the Epoch of Reionization. This quasar is among the most powerful radio emitters and the first one with direct evidence of extended radio jets ($\sim$1.6 kpc) at these high redshifts. We analyze NOrthern Extended Millimeter Array and Atacama Large Millimeter/submillimeter Array millimeter data targeting the CO (6–5) and [C II] far-infrared (FIR) emission lines, respectively, and the underlying continuum. The broad $440 \pm 80\,\mathrm{km\,s^{-1}}$ and marginally resolved [C II] emission line yields a systemic redshift of $z = 5.832 \pm 0.001$. Additionally, we report a strong 215 MHz radio continuum detection, 88 ± 7 mJy, using the Giant Metrewave Radio Telescope. This measurement significantly improves the constraints at the low-frequency end of the spectral energy distribution of this quasar. In contrast to what is typically observed in high-redshift radio-quiet quasars, we show that cold dust emission alone cannot reproduce the millimeter continuum measurements. This is evidence that the strong synchrotron emission from the quasar contributes substantially to the emission even at millimeter (FIR in the rest-frame) wavelengths. This quasar is an ideal system to probe the effects of radio jets during the formation of a massive galaxy within the first gigayear of the universe.

Unified Astronomy Thesaurus concepts: Radio loud quasars (1349); Quasars (1319); Extragalactic radio sources (508); Observational astronomy (1145); Active galactic nuclei (16); AGN host galaxies (2017); High-redshift galaxies (734)

1. Introduction

Recent observations at high redshift ($z \gtrsim 6$, or within 1 Gyr after the big bang) reveal a population of more than 300 quasars with supermassive black hole masses on the order of $\gtrsim 10^8\,M_\odot$ (e.g., Bañados et al. 2016; Wang et al. 2019) and host galaxies with star formation rates (SFRs) reaching up to 100–2500 $M_\odot\,\mathrm{yr}^{-1}$ (e.g., Decarli et al. 2018; Shao et al. 2019). The emergent picture is that the ratio of black hole mass to host galaxy mass is higher by a factor of 3–4 than expected from local relations (e.g., Venemans et al. 2016; Neeleman et al. 2021), suggesting that the black holes are growing more rapidly than their host galaxies. However, thus far all results within the first gigayear of the universe are based solely on radio-quiet quasars, since there are only 12 quasars known to be strong radio emitters at this cosmic epoch, and none of their host galaxies have been studied in the millimeter thus far (e.g., Bañados et al. 2015b, 2021; Belladitta et al. 2020; Liu et al. 2021). Hence, the role of the radio jets and their interaction with the interstellar medium (ISM) is still unexplored at these redshifts.

Quasars at $z \sim 6$ are a challenge for evolutionary models of galaxies/active galactic nuclei (AGNs), as they have to be able to form and grow billion-solar-mass black holes in less than a gigayear (e.g., Inayoshi et al. 2020). In this context, radio jets are a possible mechanism to aid such a rapid growth by enhancing the black hole accretion rates (e.g., Jolley & Kuncic 2008; Ghisellini et al. 2010, 2015; Volonteri et al. 2015; Regan et al. 2019). Furthermore, the interplay between radio jets and the ISM is thought to be an important mechanism responsible for the tight correlation between the mass of a galaxy and its central black hole (e.g., Kormendy & Ho 2013). Hydrodynamical cosmological simulations require strong AGN feedback already at $z \sim 6$ to reproduce the observed distribution of galaxy masses at $z = 0$ (e.g., Kaviraj et al. 2017). Observationally, however, evidence of AGN feedback has yet to be confirmed in sources at $z \gtrsim 6$, where both host galaxy and black hole are experiencing the first extreme and efficient growth (see also Bischetti et al. 2019; Novak et al. 2020).

[8] Fellow of the International Max Planck Research School for Astronomy and Cosmic Physics at the University of Heidelberg (IMPRS–HD).
[9] NPP Fellow.
[10] NASA Hubble Fellow.
[11] ESO Fellow.

Studying the effects that radio jets have on the stellar properties of a galaxy is challenging because the central AGN outshines the stars (e.g., Zibetti et al. 2009; Taylor et al. 2011). This is particularly difficult at high redshift, and stellar emission from host galaxies of $z \sim 6$ quasars has yet to be detected (e.g., Decarli et al. 2012; Mechtley et al. 2012; Marshall et al. 2020). Fortunately, at these redshifts key tracers of atomic and molecular gas, such as [C II] 158 μm and CO, are redshifted to the submillimeter wavelengths and thus can be observed with facilities like the Atacama Large Millimeter/submillimeter Array (ALMA) or the IRAM NOrthern Extended Millimeter Array (NOEMA). [C II] is often the brightest far-infrared (FIR) line in star-forming galaxies and can be used to infer kinematics, star formation properties, and masses of the host galaxy (e.g., Wang et al. 2013). The CO (6–5) and CO (7–6) molecular lines are expected to be among the strongest CO transitions in quasar host galaxies (e.g., Carilli & Walter 2013). Thus, the study of these tracers in radio-loud AGNs can reveal whether the jets are affecting the gas for star formation in the host galaxy.

In this paper we focus on the quasar PSO J352.4034–15.3373 (hereafter P352–15) at $z = 5.8$, discovered in Bañados et al. (2018) and confirmed to be the brightest $z \gtrsim 6$ radio object known at the time through observations with the Karl G. Jansky Very Large Array (VLA), with flux densities reaching up to ~100 mJy at ~200 MHz as measured by the Murchison Widefield Array (MWA). The only source with comparable radio luminosity at such redshift is a recently discovered blazar at $z = 6.1$ (Belladitta et al. 2020). Subsequent observations of P352–15 with the Very Long Baseline Array (VLBA) revealed the first direct evidence of extended (1.62 kpc) radio jets at $z \sim 6$ (Momjian et al. 2018). Recently, Connor et al. (2021) studied this quasar with deep (265 ks) Chandra X-ray observations, reporting an X-ray luminosity of $L_{2-10} = 1.26 \times 10^{45}$ erg s^{-1} and a structure aligned with the radio jets but at a distance of 50 kpc away, implying that the jets could affect larger scales than what is currently seen in radio emission (see Connor et al. 2021 for more details).

In this work, we present the results from follow-up analysis of P352–15 with observations at millimeter wavelengths from ALMA at 290 GHz and from NOEMA at 100 GHz. We also study the radio emission at 215 MHz with observations from the Giant Metrewave Radio Telescope (GMRT). The data reduction is described in Section 2, followed by the analysis of the continuum and emission lines in the ALMA and NOEMA observations in Section 3. We discuss the radio and FIR radiation properties in Section 4. We present our results and comparison with previous literature in Section 5. The final conclusions and discussion are presented in Section 6. Throughout this work we adopt a cosmology with $H_0 = 70$ km s^{-1} Mpc^{-1}, $\Omega_M = 0.3$, $\Omega_\Lambda = 0.7$, and $T_{\rm CMB}^{z=0} = 2.725$ K. Using this cosmology, the age of the universe is 948 Myr at the redshift of P352–15, and 1″ corresponds to 5.8 proper kpc.

2. Data

In this section we present the reduction of the data used in this work from submillimeter to radio wavelengths using ALMA, NOEMA, and GMRT.

2.1. ALMA

The target source P352–15 was observed with ALMA on 2019 November 28 as part of program 2019.1.00840.S (PI: Mazzucchelli) under median weather conditions with a mean precipitable water vapor (PWV) of 1.3 mm. The compact configuration C43-2 with a total of 44 antennas was used, resulting in maximum baselines of 314 m. Blazar J2331–1556 was used as a phase calibrator, and blazar J0006–0623 was used to calibrate the flux density scale, which is accurate within 6%. The total time on source was 756 s. The correlator was set up to observe four spectral windows using 480 channels with a channel width of 3.9 MHz for a total bandwidth of 1.875 GHz per spectral window. Two of the spectral windows were set up to have a slight spectral overlap, and together they were centered on the expected frequency of the redshifted [C II] line.

The data were calibrated with the ALMA pipeline, which is part of the common astronomy software application package (CASA; McMullin et al. 2007), using version Pipeline-CASA56-P1-B. A continuum image was made using the task *tclean* within CASA and by applying natural weighting to optimize sensitivity. For this continuum image all channels were used except for the 0.7 GHz spectral region surrounding the [C II] emission. The continuum image has an effective frequency of ≈290 GHz and an rms noise sensitivity of 0.043 mJy beam^{-1}. We also created a continuum-free line cube by removing the continuum using the task *uvcontsub*, and imaging was done with the *tclean* task. Here, we again adopted natural weighting and a channel spacing of 100 km s^{-1}. The rms noise sensitivity for this cube is 0.32 mJy beam^{-1} per 100 km s^{-1} channel. The final beam sizes for both the continuum image and line cube are elongated ellipses with FWHM major and minor axis $1\farcs3 \times 1\farcs0$ at a positional angle (PA) of 85°.6.

2.2. NOEMA

P352–15 NOEMA observations were executed to target the CO (6–5) emission line with observed frequency estimated at 101.1 GHz (program: W18EG; PIs: Eilers, Bañados). All observations were taken on 13 different visits between 2019 April 10 and May 31. The observations were taken in the receiver Band 1 (at 3 mm) in the compact configurations of 10D with 10 antennae for seven observing days, and the rest were observed in 9D configuration with nine antennae. This setup of observations was taken in compact configuration to maximize the sensitivity. Quasars 2243–123 and 2345–167 were used as phase and amplitude calibrators. The radio frequency bandpass calibrators included mostly 3C 454.3, but also 3C 84, 1749+096, and 0923+392. The star MWC 349 was used to set the absolute flux density scale, which is accurate to within 10%. The typical system temperature was (100–200) K. The precipitable water vapor conditions were mostly within PWV ~ 2–5 mm and with only four visits extending up to PWV ~ 10 mm. Due to the elevation of our source, there was often shadowing, mainly in Antenna 4 and Antenna 1. The total nine-antenna equivalent time on source is 12.2 hr.

The data were reduced at IRAM with the software CLIC and MAPPING from the GILDAS suite,[12] and the final cube was analyzed in Python. Two cubes with resolutions of 300 and 100 km s^{-1} were made to identify and analyze the CO (6–5) emission line and the underlying continuum. For both cubes, imaging was performed using natural weighting in order to maximize sensitivity, and cleaning was done with the simplest Hogbom algorithm. The cube with 300 km s^{-1} channel spacing has an rms noise of 0.10 mJy beam^{-1} per channel and a

[12] https://www.iram.fr/IRAMFR/GILDAS/

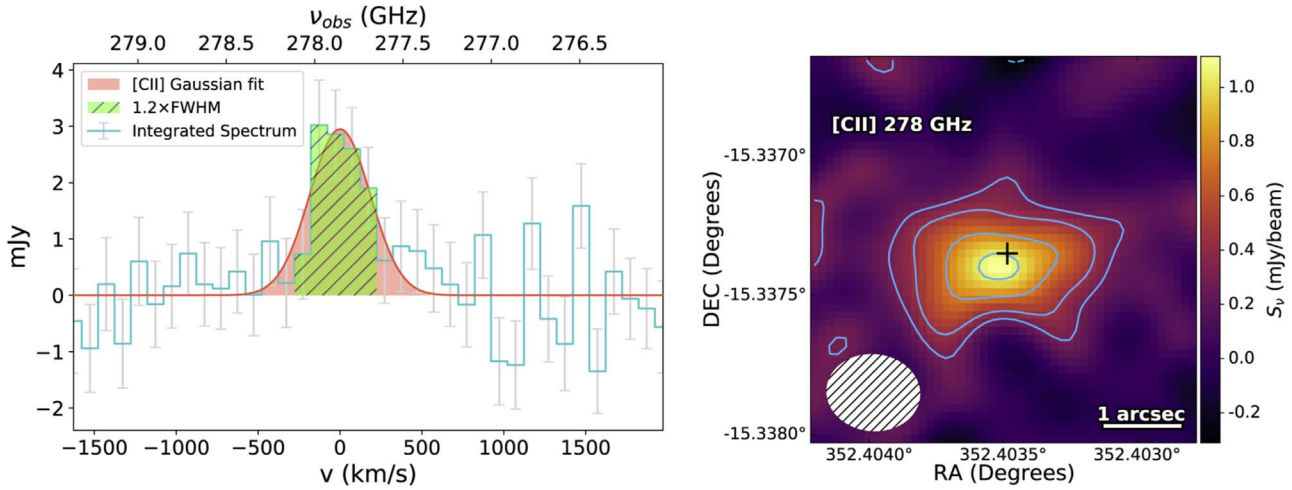

Figure 1. Left: ALMA continuum-subtracted [C II] emission of P352–15. We use a 1.″7-aperture radius to extract the emission-line spectra presented here in blue. The error bars represent the rms within the aperture at each channel. The spectral range used for the Gaussian fit of [C II] is shaded in orange and corresponds to a velocity-integrated value of 1.37 ± 0.22 Jy km s^{-1}. The [C II] fit at peak has a flux density of 2.95 ± 0.48 mJy. The hatched area in green corresponds to $\approx 1.2 \times$ FWHM of the Gaussian fit and is used to create the [C II] map shown in the right panel. Right: 2D map of [C II] built with the data from the channels shown in the left panel in green. The emission is marginally resolved, and the contour levels are shown at $(-2\sigma, 2\sigma, 3\sigma, 5\sigma, 7\sigma)$ with $\sigma = 0.15$ mJy beam^{-1}, where the beam is 1.″3 × 1.″0. The [C II] line is detected at S/N > 7.5. The plus sign is centered at the optical position of P352–15 from Momjian et al. (2018).

synthesized beam size of 7.″3 × 3.″8 and PA of 5.°44. The second cube has an rms of $\sigma = 0.18$ mJy beam^{-1} per 100 km s^{-1} channel. This cube has a beam size of 7.″3 × 3.″7 and PA of 5.°41.

2.3. GMRT

P352–15 was detected in the GaLactic and Extra-galactic All-sky MWA (GLEAM) survey and the TIFR GMRT Sky Survey (TGSS) at low frequencies (150–200 MHz). However, the cataloged flux densities in this range show a wide scatter, with the GLEAM data consistent with 80–120 mJy at 200 MHz (Hurley-Walker et al. 2017). The TGSS image shows significant imaging artifacts (stripes), and our reanalysis of the image finds a peak of 110 mJy beam^{-1} but a total flux density (significantly affected by the stripes) of 169 mJy (Intema et al. 2017; de Gasperin et al. 2018).

To clarify the source flux density at low frequency, we observed the source with the GMRT at 215 MHz on 2018 June 23, for 4 hr. The observations were centered at 215.5 MHz, with a bandwidth of 25 MHz using 16,384 channels, for interference excision. The flux density scale was set assuming 52.3 Jy for 3C 48 at 215 MHz (Perley & Butler 2017). Delay and bandpass calibrations were also performed using 3C 48. The array gain and amplitudes were tracked in time using the calibrator J2321–163, which had a bootstrapped flux density (from 3C 48) of 14.0 Jy. All calibrations were done using standard procedures in CASA (McMullin et al. 2007). Interference was substantial, in particular on short baselines, and the final calibration and analysis employed only baselines longer than 1.5 km.

The final imaging used CASA task CLEAN with Briggs weighting with a robust factor = 0 (Briggs et al. 1999). The resulting synthesized beam was = 18″ × 11″, with PA = −48°. The rms noise on the final image is 4 mJy beam^{-1}. The source was easily identified as seen in Figure 3. Gaussian fitting indicated that the source was unresolved, with a flux density of 88 ± 7 mJy, whose uncertainty is dominated by the estimated 8% error from the the absolute flux density bootstrap calibration process.

Table 1
Measurements from Line Emission Search

$S_{[C\ II]}$	2.95 ± 0.48 mJy
$S_{[C\ II]}\ \Delta v$	1.37 ± 0.22 Jy km s^{-1}
FWHM$_{[C\ II]}$	440 ± 80 km s^{-1}
EW$_{[C\ II]}$	2.12 ± 0.42 μm
$z_{[C\ II]}$	5.832 ± 0.001
$S_{CO\ (6-5)}$	<0.35 mJy

3. Emission-line Search and Millimeter Continuum Measurements

In this section we present a detailed analysis of P352–15 in ALMA and NOEMA data with the purpose of measuring the [C II] and CO (6–5) lines and their underlying continuum properties (see Table 1).

3.1. [C II] Line and 290 GHz Continuum

We use the ALMA continuum-free line cube generated in Section 2.1 to look for the [C II] line. We find that the line is consistent with the expected redshift $z \sim 5.84$ and looks spatially resolved to some extent. Therefore, we perform an aperture photometry test at varying apertures from 1.″0 to 2.″0. We perform a Gaussian fit to the [C II] spectrum and search for the aperture at which the velocity-integrated [C II] emission begins to plateau. This turning point occurs at a radial aperture of 1.″7. The resulting continuum-subtracted [C II] spectrum is shown in Figure 1, which is the [C II] spectrum used in the remaining analysis.

From the Gaussian fit, we find that the [C II] emission line has an FWHM of 440 ± 80 km s^{-1} and the line peaks at an observed frequency of 278.20 ± 0.03 GHz (see Figure 1, left). Using this value and the rest-frame frequency of [C II] (1900.5369 GHz; Schöier et al. 2005), we calculate the systemic redshift of P352–15 to be $z = 5.832 \pm 0.001$. The flux density peak is 2.95 ± 0.48 mJy, and the velocity-integrated line is 1.37 ± 0.22 Jy km s^{-1}. To generate a [C II] map, we reimaged the data cube using channels within 1.2 × FWHM of the [C II] emission line, which, given our

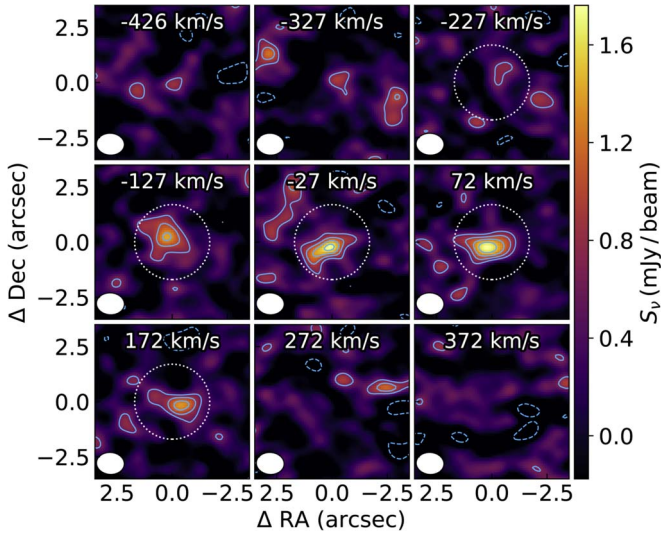

Figure 2. ALMA 278 GHz [C II] emission in 100 km s^{-1} channel maps of P352–15. The central map corresponds to the channel closest to the peak velocity at -372.57 ± 34.91 km s^{-1} from the fitted [C II] emission model (orange zone in Figure 1). For each panel, the central coordinates correspond to R.A. (J2000) = $23^{h}\,29^{m}36\overset{s}{.}8363$, decl. (J2000) = $-15°20'14\overset{''}{.}460$, the channel velocities relative to the the peak velocity are given at the top, and the synthesized beams are shown in the lower left corner. The channels used for flux extraction are presented with a white dotted circle of $1\overset{''}{.}7$ aperture radius. In all maps the contour levels are shown at (-2σ, 2σ, 3σ, 4σ, 5σ), with their respective σ values ~0.03 mJy beam^{-1}.

observations, corresponds to the green shaded channels in Figure 1. Using this channel spacing maximizes the signal-to-noise ratio (S/N) on the emission line and recovers 84% of the flux emission, assuming that it is Gaussian (see Appendix A in Novak et al. 2020). The [C II] map is shown in the right panel of Figure 1 and has an rms of 0.15 mJy beam^{-1}. We note that the beam size is $1\overset{''}{.}3 \times 1\overset{''}{.}0$ and therefore does not resolve the radio jet revealed by the VLBA, which extends over $0\overset{''}{.}28$ (see Momjian et al. 2018).

The [C II] map shows an extended morphology that we fit with a 2D Gaussian profile using CASA. The result is a deconvolved source with major and minor axes of sizes $2\overset{''}{.}0 \times 0\overset{''}{.}8$ and position angle 96°, confirming that the [C II] emission of the quasar host galaxy is marginally resolved. Thus, we decide to investigate its morphology from channel to channel. Figure 2 shows the ALMA channel maps for P352–15 around the observed frequency of [C II], with the dotted white circles denoting the channels and spatial regions used to extract the [C II] flux emission and create the 2D map shown in Figure 1. The central panel shows the [C II] emission closest to the peak velocity from the Gaussian fit (-372.57 ± 34.91 km s^{-1}) at -27 km s^{-1} away. This channel and the 72 km s^{-1} centered channel (middle right panel) have the highest S/N, with S/N > 5. At the spatial resolution and S/N of our observations there are no significant changes in morphology per channel. The current data are insufficient to draw any conclusions on galaxy dynamics. Higher spatial resolution and S/N observations are needed to investigate the true velocity structure of the [C II] emission line in this quasar host galaxy.

Finally, we utilize the reduced ALMA continuum cube (refer to Section 2.1) to measure the underlying continuum at 290 GHz. The emission is unresolved with a flux density of 0.34 ± 0.04 mJy (see Figure 3, top).

3.2. CO (6–5) Line and 100 GHz Continuum

We use the resampled NOEMA cubes at 300 and 100 km s^{-1} described in Section 2.2 to search for the CO (6–5) molecular emission line. We do not find a significant detection of the line in either of the cubes. In order to estimate an upper limit on the CO (6–5) luminosity, we use the cube with the 100 km s^{-1} velocity increment and assume that the line has the same FWHM as the measured [C II] emission line. We find a 3σ upper limit of 0.35 mJy, which corresponds to $L_{\mathrm{CO\ (6-5)}} < 0.5 \times 10^9\ L_\odot$. This upper limit is comparable to the median values for CO (6–5) measured in $z > 6$ radio-quiet quasars (e.g., Venemans et al. 2017a). The 100 GHz continuum emission is clearly detected and unresolved with a flux density of 0.10 ± 0.01 mJy (Figure 3).

4. The Spectral Energy Distribution of P352–15

We build the spectral energy distribution (SED) for P352–15 by making use of the data presented in this paper and previously reported optical data from Gemini/GMOS r'; Pan-STARRS1 *i*, *z*, *y* bands; and Magellan/FourStar *J* band, as well as radio observations with the VLA at 3.0 and 1.4 GHz (see Bañados et al. 2018; Connor et al. 2021). In the following subsections, we will investigate the FIR properties of the quasar and will refine its radio properties. We summarize all existing measurements in Table 2 and Figure 4.

4.1. Modeling the Radio Emission

The radio continuum spectrum is dominated by synchrotron emission at rest-frame frequencies $\lesssim$10 GHz, where the thermal bremsstrahlung (free–free) emission is weak (Duric et al. 1988). Free–free emission becomes significant at higher frequencies, which for this quasar results in a negligible contribution ($\ll 1$ μJy) for the study of the SED (e.g., Yun & Carilli 2002; Venemans et al. 2017a). As shown in Figure 4, the synchrotron radiation of P352–15 is well described as a simple power law of the form $S_\nu \propto \nu^\alpha$, where S_ν is the observed flux density at the frequency ν and α is the radio spectral index. In Bañados et al. (2018) the synchrotron power-law slope was not well constrained because of the large scatter at the lower-frequency observations. Bañados et al. (2018) assumed two cases for their analysis with radio slope index $\alpha_{1.4}^{0.150} = -0.89$ and -1.06. With our higher-S/N GMRT data (see Section 2.3), we can obtain a more robust measurement of the synchrotron radio slope. We fit a power law to the data from observed frequencies 3 GHz, 1.4 GHz, and 215 MHz, resulting in a radio spectral index of $\alpha_3^{0.215} = -0.88 \pm 0.08$.

The new spectral index presented here allows for an improved calculation of the radio-loudness of P352–15. We adopt the definitions for radio-loudness, for which a quasar is considered radio-loud when $R_{4400} = f_{\nu,5\ \mathrm{GHz}}/f_{\nu,4400\ \mathring{A}} > 10$ or $R_{2500} = f_{\nu,5\ \mathrm{GHz}}/f_{\nu,2500\ \mathring{A}} > 10$ (Sramek & Weedman 1980; Kellermann et al. 1989). From our power-law fit we calculate a flux density of 3.87 ± 0.10 mJy at rest frame 5 GHz. We use the $L_{4400\ \mathring{A}}$ reported in Bañados et al. (2018) and convert it to flux density and find f_ν, 4400 Å $= (3.53 \pm 0.89) \times 10^{-3}$ mJy. We therefore calculate the radio-loudness $R_{4400} = 1100 \pm 280$, which agrees with the $R_{4400} \gtrsim 1000$ reported in Bañados et al. (2018). Similarly, from the $L_{2500\ \mathring{A}}$ we calculate $f_{\nu,2500\ \mathring{A}} = (2.63^{+0.19}_{-0.16}) \times 10^{-3}$ mJy and measure $R_{2500} = 1470^{+110}_{-100}$. Although the radio-loudness of P352–15 is extreme and similar to those observed in blazars (e.g., Romani et al. 2004; Sbarrato et al. 2012; Belladitta et al. 2019, 2020), its X-ray properties (Connor et al. 2021) confirm its

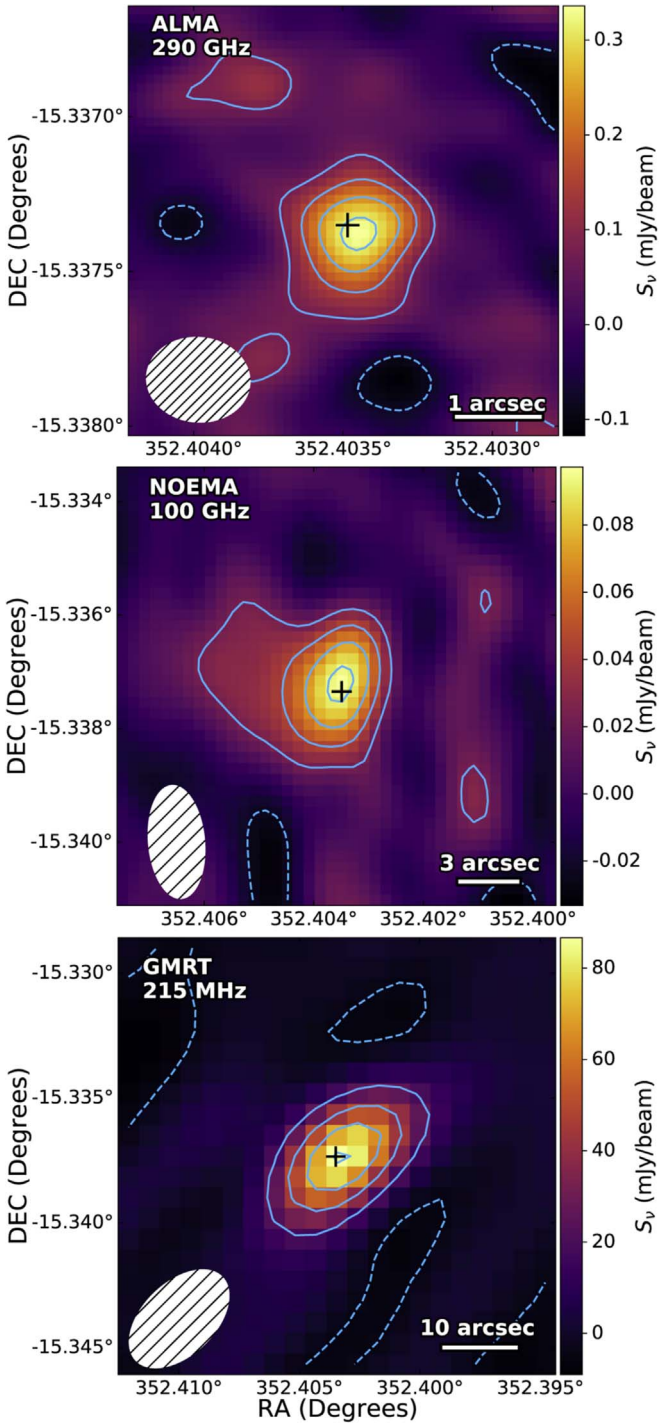

Figure 3. Top: ALMA 290 GHz continuum emission map of P352–15, with an rms $\sigma = 0.04$ mJy beam^{-1}. The beam size is $1\farcs3 \times 1\farcs0$, and the quasar is unresolved. Middle: NOEMA 100 GHz continuum emission map with $\sigma = 0.01$ mJy beam^{-1}. The beam size is $7\farcs3 \times 3\farcs7$, and the quasar is unresolved. Bottom: GMRT 215 MHz emission map with a beam size of $18'' \times 11''$ and $\sigma = 4$ mJy beam^{-1}. The quasar appears unresolved. The contour levels for ALMA and NOEMA maps are shown at $(-2\sigma, 2\sigma, 4\sigma, 6\sigma, 8\sigma)$, and both have S/N > 8. The GMRT continuum has contours shown at $(-1\sigma, 5\sigma, 10\sigma, 15\sigma, 20\sigma)$ and has S/N > 20. For all maps, the dashed and solid contours represent the negative and positive σ, respectively. The plus sign in all panels is centered at the optical position of P352–15 from Momjian et al. (2018).

quasar nature. The parameters of the X-ray-to-optical index $\alpha_{ox} = -1.45 \pm 0.11$ and the photon index $\Gamma = 1.99^{+0.29}_{-0.28}$ fall under the quasar classification although near the threshold of high-redshift blazars from Ighina et al. (2019), where a blazar has $\tilde{\alpha}_{ox} < 1.355$[13] and $\Gamma < 1.8$. Typically, the photon index is $\Gamma \geqslant 1.5$ for high-redshift quasars even up to $z \gtrsim 6$ (e.g., Nanni et al. 2018). Additionally, the radio jet orientation of P352–15 not pointing along our line of sight (Momjian et al. 2018), and the steep radio slope ($\alpha_3^{0.215} = -0.88 \pm 0.08$; see Figure 4) are inconsistent with this quasar being a blazar.

Table 2
Flux Densities and Derived Properties of P352–15

Telescope/Band	Central λ/ν	Flux Density
Gemini-N/GMOS r	630 nm	0.17 ± 30 μJy
Pan-STARRS1 i_{P1}	752 nm	1.8 ± 0.5 μJy
Pan-STARRS1 z_{P1}	866 nm	11.8 ± 0.7 μJy
Pan-STARRS1 y_{P1}	962 nm	13.6 ± 1.5 μJy
Magellan/FourStar J	1242 nm	14.6 ± 0.4 μJy
ALMA Band-7	290 GHz	0.34 ± 0.04 mJy
NOEMA Band 1	100 GHz	0.10 ± 0.01 mJy
VLA-S	3 GHz	8.20 ± 0.25 mJy
VLA-L	1.4 GHz	14.9 ± 0.7 mJy
GMRT Band-235 MHz	215 MHz	88 ± 7 mJy
Rest-frame Luminosity L ($L_\odot$)		
$L_{5\ \mathrm{GHz}}$		$10^{10.28\pm0.01}$
$L_{4400\ \text{Å}}$		$10^{12.37\pm0.11}$
$L_{2500\ \text{Å}}$		$10^{12.49\pm0.03}$
Radio-loudness		
R_{4400}		1100 ± 280
R_{2500}		1470^{+110}_{-100}

4.2. Modeling the Millimeter Emission

In this work we present two millimeter-continuum measurements of P352–15 from ALMA 290 GHz and NOEMA 100 GHz observations with S/N > 8 (see Figure 3), corresponding to the quasar's rest-frame frequencies of 1981 and 683 GHz, respectively. The flux densities at these frequencies are consistent with being at the Rayleigh–Jeans tail (optical depth $\tau_{\mathrm{Dust}} \ll 1$) of a modified blackbody function (MBB), thought to be a good representation of cold dust from the quasar host galaxy (e.g., Priddey & McMahon 2001; Beelen et al. 2006; da Cunha et al. 2013; Leipski et al. 2014; Venemans et al. 2016, 2018). The Planck function is

$$B_{\nu_{\mathrm{rest}}}(T_{\mathrm{Dust},z}) = \frac{2h\nu_{\mathrm{rest}}^3/c^2}{e^{(h\ \nu_{\mathrm{rest}}/k\ T_{\mathrm{Dust},z})} - 1}, \quad (1)$$

where $T_{\mathrm{Dust},z}$ is the dust temperature at a given redshift. Typical dust parameters of the MBB found for host galaxies of radio-quiet quasars are $T_{\mathrm{Dust}} = 47$ K and dust emissivity spectral index $\beta = 1.6$ (e.g., Beelen et al. 2006; Venemans et al. 2016). In the following analysis we will assume these best-fit parameters and check whether they represent the properties of this quasar known to have strong radio emission. Later on, we will also explore whether different values of T_{Dust} and β can provide a better representation of the existing data of P352–15.

[13] $\tilde{\alpha}_{ox} = 0.789\alpha_{ox} + 0.212(\Gamma - 1.0)$.

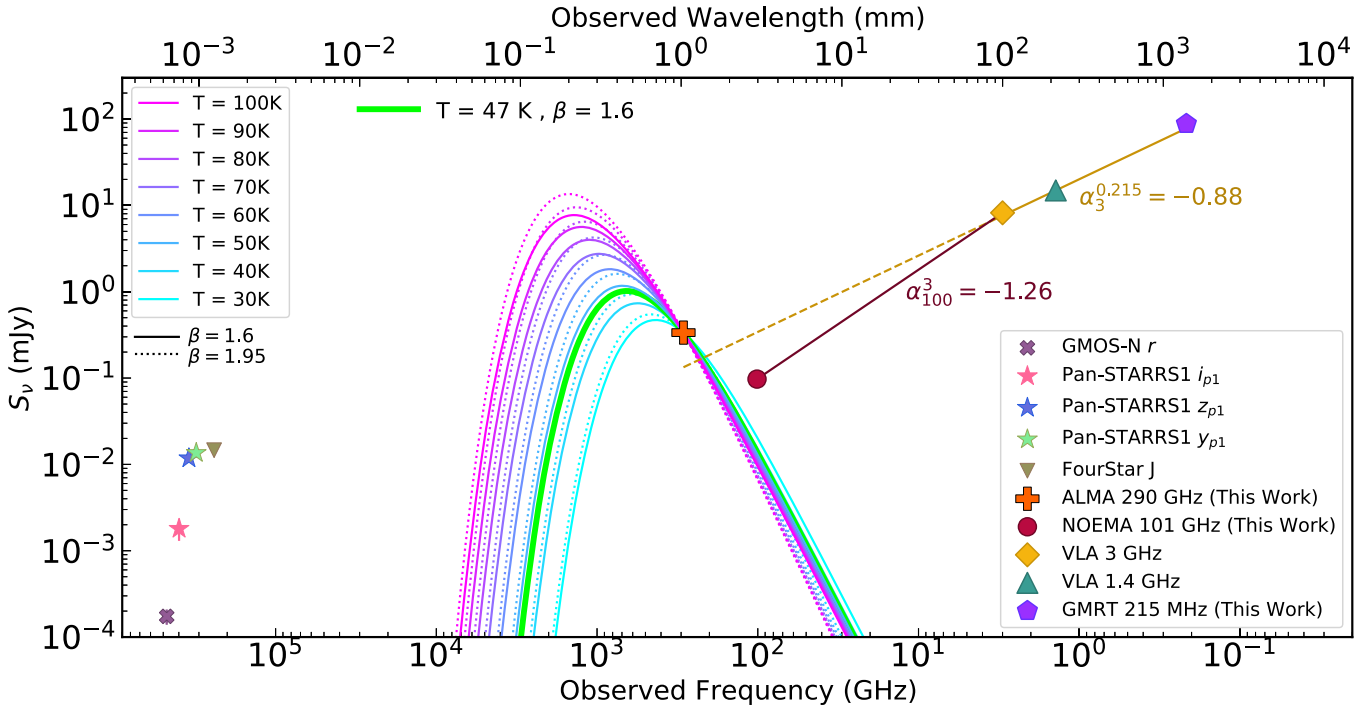

Figure 4. Optical, millimeter, and radio SED of P352–15 at $z = 5.832$. The millimeter ALMA and NOEMA measurements are inconsistent with cold dust modeled as a modified blackbody at different dust temperatures and dust emissivity spectral indexes. The radio data at 215 MHz–3 GHz are well described by synchrotron emission with a power-law slope $\alpha = -0.88$. However, extrapolating that power law (dashed line) would be inconsistent with the millimeter data. To explain this SED, the synchrotron emission must steepen or break at high frequencies. We note that the error bars from the measurements are small compared to the scale of the figure and thus are not shown in the image.

The predicted observed flux density from dust heating can be calculated with the MBB following Novak et al. (2019):

$$S_{\rm obs} = f_{\rm CMB}\ [1 + z]\ D_L^{-2}\ \kappa_{\nu_{\rm rest}}(\beta) M_{\rm Dust}\ B_{\nu_{\rm rest}}(T_{{\rm Dust},z}). \quad (2)$$

Here $f_{\rm CMB}$ is a correction against the cosmic microwave background (CMB) contrast; D_L is the luminosity distance; $\kappa_{\nu,{\rm rest}}(\beta)$ is the dust mass opacity, which depends on the dust emissivity spectral index β; and $M_{\rm Dust}$ is the dust mass. All values are given in SI units.

The $f_{\rm CMB}$ term corrects for CMB contrast and heating effects, which can be significant at these high redshifts, as we are seeing fluxes at frequencies close to the peak of the CMB (see da Cunha et al. 2013). However, we do not include a CMB heating correction in Equation (2), as this effect is still not significant for $T_{\rm Dust,0} = 30$–100 K at $z = 5.832$ (including CMB heating changes the temperature in that range by <0.3 K). Thus, $f_{\rm CMB}$ in Equation (2) is only the correcting factor for CMB contrast, where the blackbody calculated with the temperature of the CMB at the redshift of the source is divided by the blackbody at the dust temperature:

$$f_{\rm CMB} = 1 - \frac{B_{\nu_{\rm rest}}\ (T_{{\rm CMB},z})}{B_{\nu_{\rm rest}}\ (T_{{\rm Dust},z})}. \quad (3)$$

For $z = 5.832$ and $T_{\rm Dust} = 47$ K, $f_{\rm CMB}$ corresponds to 0.96 and 0.79 for the ALMA 290 GHz and NOEMA 100 GHz continuum points, respectively.

We assume for $\kappa_{\nu,{\rm rest}}(\beta)$ the relation derived in the submillimeter at 850 μm in Dunne et al. (2000) and James et al. (2002):

$$\kappa_{\nu_{\rm rest}}(\beta) = 0.077\ (\nu_{\rm rest}/352\ {\rm GHz})^{\beta}\ {\rm m^2\ kg^{-1}}. \quad (4)$$

We scale the MBB (Equation (2)) to match the observed ALMA 290 GHz continuum and obtain a dust mass value of $(0.36 \pm 0.04) \times 10^8\ M_\odot$. We note that if, instead of using Equation (4), we assume $\kappa_{\nu,{\rm rest}} = 2.64\ {\rm m^2\ kg^{-1}}$ at $\nu_{\rm rest} = c/(125\ \mu{\rm m})$ as presented in Dunne et al. (2003), the value of $M_{\rm Dust}$ would decrease by a factor of 1.6.

Using the calculated dust mass value and Equation (2), we can model the MBB at different frequencies. This model predicts a flux density of 0.0139 mJy at 100 GHz, while our NOEMA measurement is 0.10 mJy. Therefore, these values are inconsistent by an order of magnitude and are 7.6σ off from the observed NOEMA flux density. Since neither value set is able to fit the MBB function to both ALMA and NOEMA continuum measurements, we explore the different MBB functions that can be obtained when varying $T_{\rm Dust} = 30$–100 K and $\beta = 1.6$ and $\beta = 1.95$ as shown in Figure 4. We also try to find a β value that could fit both of our millimeter-continuum points. This results in $\beta = -0.7$; however, such a negative dust emissivity index has never been reported for dust in galaxies (see, e.g., Dunne et al. 2000; Beelen et al. 2006).

It is evident that none of these models can reproduce our data, implying that in this system the millimeter emission not only is due to cold dust but also must be affected by an additional source, the main suspect being the strong synchrotron emission of the quasar, as discussed below.

5. Discussion

In this section we discuss the implications of our results for the intriguing SED of the radio-loud quasar P352–15. We first describe the possible influence of synchrotron emission up to higher frequencies, which are usually dominated by dust continuum. Next, we report the derived FIR properties for the quasar based on the millimeter continuum measured with

ALMA at 290 GHz, assuming that this measurement is not contaminated by synchrotron radiation.

5.1. Effects of the Synchrotron Emission on the Millimeter Continuum Measurements

From the observations described in this work, we see that the radio spectrum is clearly defined by the power-law slope of $\alpha_3^{0.215} = -0.88 \pm 0.08$. However, the continuum emission at millimeter wavelengths is not well matched to a blackbody fit (Figure 4). Given the strong radio emission in this quasar, a possible explanation would be that the millimeter emission is highly affected by synchrotron radiation instead of being only due to cold dust (e.g., Weiß et al. 2008).

In order to assess this possibility, we use the synchrotron power-law fit derived in Section 4.1 and extrapolate it to the millimeter data points. We would expect the extrapolated flux at 100 GHz to be above the measured NOEMA continuum, but the flux density at 290 GHz would be below the measured ALMA continuum (see dashed line in Figure 4). When evaluating the slope between the VLA 3 GHz and NOEMA 100 GHz flux density values, the observed spectral index is much steeper ($\alpha_{100}^3 = -1.26 \pm 0.03$) than $\alpha_3^{0.215}$. This means that, extrapolating the synchrotron power law, we would have expected a NOEMA detection about three times brighter than what we measure. Therefore, it is very likely that the 100 GHz emission in this quasar is dominated by synchrotron emission. Further measurements between 3 and 100 GHz are required to pinpoint the location of an expected spectral break.

Extrapolating the synchrotron power law ($\alpha_3^{0.215} = -0.88$) all the way to 290 GHz results in 0.13 mJy. This implies that the synchrotron contribution in the ALMA measurement could be up to 40% of the measured value. However, this is a strict upper limit given that we know that there is a break in the power-law spectrum between 3 and 100 GHz (Figure 4). If we extrapolate to 290 GHz using the $\alpha_{100}^3 = -1.26$ power law, we expect a synchrotron contribution of only 8% in the ALMA continuum measurement.

Due to the significant synchrotron contribution for the NOEMA 100 GHz observations and a smaller influence on the ALMA 290 GHz, we explore an overall fit of the synchrotron emission and the cold dust, to model both components of the SED simultaneously from the radio to millimeter regime. For this purpose, we tried to fit the MBB function and a simple power-law function, but this model cannot reproduce our data. We then performed a joint fit using an MBB and a broken power law and fix the break frequency at 3 GHz, which is the limit of our observations in radio. The resulting model is overfitted given the few data points, and the fitted parameters do not yield trusting values. Since more observations at complementary frequencies are needed to determine the break frequency, we continue to constrain the two components in millimeter and radio separately.

5.2. FIR Properties of P352–15

We use the ALMA continuum measurement to estimate the dust properties of the host galaxy, assuming that the synchrotron emission at this frequency is minimal. However, we caution the reader that these measurements should be considered as upper limits given that a nonnegligible contribution from the synchrotron emission is possible. Additional measurements covering the 3–100 GHz gap are required to better disentangle the synchrotron emission at this frequency.

Table 3
Derived FIR Properties for P352–15

$M_{\rm Dust}$[a]	$(0.36 \pm 0.04) \times 10^8\ M_\odot$
$L_{\rm FIR}$[a]	$(0.89 \pm 0.10) \times 10^{12}\ L_\odot$
$L_{\rm TIR}$[a]	$(1.26 \pm 0.15) \times 10^{12}\ L_\odot$
$\rm SFR_{TIR}$[a]	$(110.0 \pm 13.0)\ M_\odot\ \rm yr^{-1}$
$L'_{\rm [C\,II]}$	$(5.6 \pm 0.9) \times 10^9\ \rm K\ km\ s^{-1}\ pc^2$
$L_{\rm [C\,II]}$	$(1.23 \pm 0.20) \times 10^9\ L_\odot$
$\rm SFR_{[C\,II]}$[b]	$(54–285)\ M_\odot\ \rm yr^{-1}$
$L_{\rm [C\,II]}/L_{\rm FIR}$	$(1.38 \pm 0.23) \times 10^{-3}$
$L_{\rm CO\ (6-5)}$	$<0.5 \times 10^9\ L_\odot$

Notes.
[a] These values are calculated assuming an MBB matched to the ALMA continuum with $T_{\rm Dust} = 47$ K and $\beta = 1.6$. We caution that these measurements might be affected by synchrotron emission.
[b] Calculation using the SFR-to-luminosity relation derived in De Looze et al. (2014).

From the $M_{\rm Dust}$ derived in Section 4.2, along with the dust parameters $T = 47$ K and $\beta = 1.6$, we integrate over the SED and obtain infrared luminosity constraints. We calculate the FIR luminosity by integrating over rest frame 42.5–122.5 μm and get $L_{\rm FIR} = (0.89 \pm 0.10) \times 10^{12}\ L_\odot$. Integrating over the rest-frame wavelengths 8–1000 μm, we obtain the total infrared (TIR) luminosity as $L_{\rm TIR} = (1.26 \pm 0.15) \times 10^{12}\ L_\odot$. We derive an SFR from the $L_{\rm TIR}$ following the relation in Kennicutt & Evans (2012) scaled to the Chabrier (2003) initial mass function (IMF; this results in an SFR 1.7 times smaller than assuming the Salpeter 1955 IMF), obtaining $\rm SFR_{TIR} = (110.0 \pm 13.0)\ M_\odot\ yr^{-1}$. This value is ∼15% smaller than that resulting from calibrations in Kennicutt (1998). The uncertainty in $\rm SFR_{TIR}$ can be larger because we cannot constrain the dust parameters for temperature T and emissivity index β (see Figure 4).

Using the equations for calculating line luminosities from [C II] measurements presented by Carilli & Walter (2013), we find the areal integrated source brightness temperature $L'_{\rm [C\,II]} = (5.6 \pm 0.9) \times 10^9\ \rm K\ km\ s^{-1}\ pc^2$. The [C II] line luminosity, which is commonly used to compare luminosities to the underlying continuum, is $L_{\rm [C\,II]} = (1.23 \pm 0.20) \times 10^9\ L_\odot$. We use the relation in De Looze et al. (2014) to calculate the [C II]-derived SFR:

$$\log \rm SFR_{[C\,II]} = -6.09 + 0.90 \times \log L_{[C\,II]}. \quad (5)$$

Taking into account the systematic uncertainty in this relation of a factor ∼2.3, we find $\rm SFR_{[C\,II]} = 54–285\ M_\odot\ yr^{-1}$, which is consistent with the SFR inferred from the TIR luminosity, as indicated in Table 3.

5.3. Comparison with the Literature

Here we place the [C II] and dust emission properties for P352–15 in the context of other quasars at $z \gtrsim 6$ in the literature. In Figure 5, we compile the properties of $z \gtrsim 6$ quasars with continuum measurements of $\rm S/N > 3$ as reported by Decarli et al. (2018), Izumi et al. (2018), Eilers et al. (2020, 2021), and Venemans et al. (2020). We note that all the literature quasars are radio-quiet, with the only exception being J2318–3113, whose [C II] properties have been studied by Decarli et al. (2018) and Venemans et al. (2020), but it was only recently identified as radio-loud (with $R_{4400} \sim 70$) by

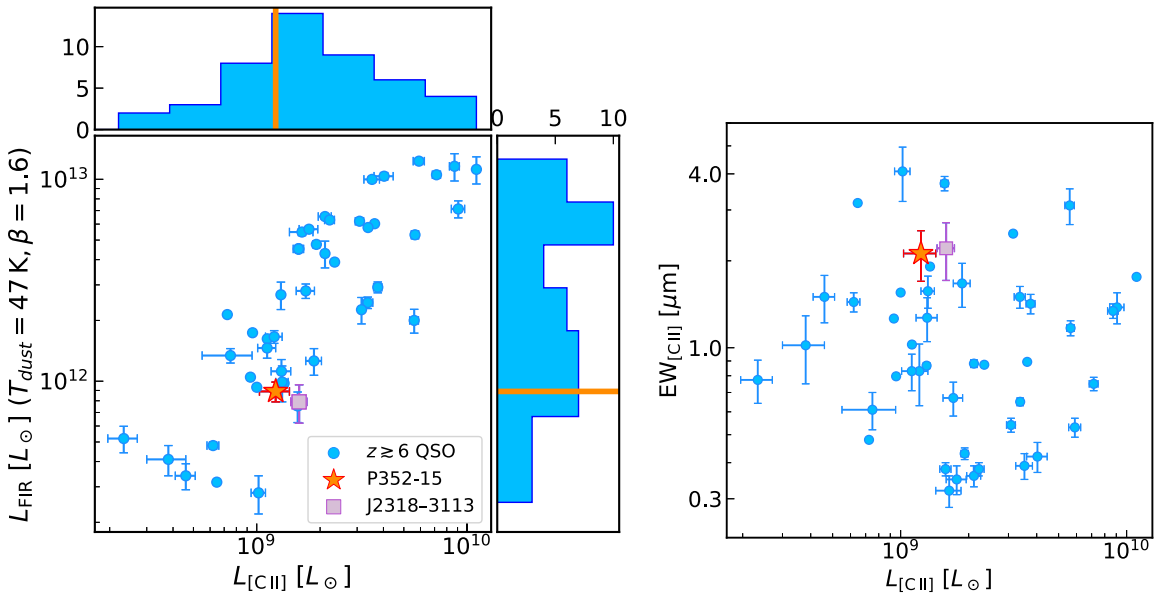

Figure 5. Left: relationship between the FIR luminosity (assuming that it is dominated by cold dust with $T_{\rm Dust} = 47$ K and $\beta = 1.6$) and the [C II] luminosity reported in 45 $z \gtrsim 6$ quasars from Decarli et al. (2018), Izumi et al. (2018), Eilers et al. (2020, 2021), and Venemans et al. (2020). The derived properties of P352–15 are within typical values for $L_{\rm FIR}$ and $L_{\rm [C\,II]}$ in context with the literature. Right: comparison between the [C II] equivalent width and the [C II] luminosity using the same sample of $z \gtrsim 6$ quasars. P352–15's EW$_{\rm [C\,II]}$ value is at the high end of the distribution found in the literature. The two panels also highlight J2318–3113, the only other radio-loud quasar in the $z \gtrsim 6$ sample with available information for comparison. Both radio-loud quasars have very similar [C II] and FIR properties.

Ighina et al. (2021). Both radio-loud quasars with [C II] information, P352–15 and J2318–3113, are highlighted in Figure 5.

P352–15 has a [C II] line width of 440 ± 80 km s^{-1}, which is broader but within one standard deviation than the mean of the distribution from $z \gtrsim 6$ quasars in the literature (350 ± 125 km s^{-1}; Decarli et al. 2018; Venemans et al. 2020). The [C II] luminosity we calculate for P352–15 is $(1.23 \pm 0.20) \times 10^9\ L_\odot$, which is smaller than the median of the distribution but is still within the typical values of (1–5) $\times 10^9\ L_\odot$ for quasars at $z \gtrsim 6$ (see Figure 5 and, e.g., Mazzucchelli et al. 2017; Venemans et al. 2017b; Novak et al. 2019).

As mentioned in Section 4, the dust properties for quasar P352–15 cannot be fully constrained given the strong synchrotron contamination at millimeter wavelengths. However, we see that the upper limit estimate for $L_{\rm FIR} \sim 10^{12}\ L_\odot$ overlaps with those of quasar host galaxies at $z \gtrsim 6$ in the literature, although it is smaller than the median value of the population (Figure 5). Similarly, the SFR implied by the total infrared emission is consistent with the one we derive from the [C II] line and with previous studies of quasars at these redshifts (e.g., Mazzucchelli et al. 2017; Eilers et al. 2020, 2021).

A widely used diagnostic to study properties of the ISM is the [C II]-to-FIR luminosity ratio. Local galaxies ($z < 1$) show a decrease in this ratio toward higher FIR luminosities (referred to as the "[C II] deficit"), driven by the presence of mechanisms provoking dust heating in the ISM (e.g., Malhotra et al. 2001; Farrah et al. 2013; Sargsyan et al. 2014; Díaz-Santos et al. 2017). The high-redshift ($z \gtrsim 6$) sample has a large scatter for this ratio, but our calculated $\log(L_{\rm [C\,II]}/L_{\rm FIR}) = -2.86$ is comparable to local ultraluminous infrared galaxies and is consistent with previously found measurements of $z > 6$ quasars (see trend in Figure 5, left; e.g., Venemans et al. 2012, 2017b; Bañados et al. 2015a; Willott et al. 2015; Mazzucchelli et al. 2017; Decarli et al. 2018).

A useful quantity to investigate is the [C II] equivalent width (EW), which has the advantage that it does not depend on the shape of the dust SED:

$$\frac{\rm EW}{[\mu{\rm m}]} = 1000\ \frac{S\Delta v\,[{\rm Jy\ km\ s^{-1}}]}{S_{\nu,0}({\rm cont})\,[{\rm mJy}]}\ \frac{\lambda_0[\mu{\rm m}]}{c\,[{\rm km\ s^{-1}}]}. \quad (6)$$

Here $S\Delta v$ is the velocity-integrated line; $S_{\nu,0}$(cont) is the observed continuum flux density at the rest-frame frequency of the line ([C II] in this case); λ_0 is the rest wavelength, which for [C II] is 157.74 μm; and c is the speed of light. Our computed value for P352–15 is EW$_{\rm [C\,II]} = 2.12 \pm 0.42$ μm, placing P352–15's EW$_{\rm [C\,II]}$ at the high end of the distribution, but with several other hosts of radio-quiet quasars having comparable or larger EW$_{\rm [C\,II]}$ (see right panel of Figure 5). We conclude that the EW$_{\rm [C\,II]}$ of P352–15 is consistent with what is expected from the properties of radio-quiet quasars, and it is therefore likely that the continuum underlying the [C II] emission is indeed not strongly influenced by the radio emission (see Section 5.1).

It is worth noting that the only two $z \gtrsim 6$ radio-loud quasars studied in their rest-frame FIR and [C II] properties lie in a very similar position in the parameter space of Figure 5. Nevertheless, a systematic millimeter study of a larger sample of radio quasars at high redshifts is necessary to be able to make statistical comparisons between the black hole/host galaxy properties of radio-loud and radio-quiet sources.

6. Summary and Conclusions

We present and analyze millimeter and radio observations of the powerful radio bright quasar P352–15. Our major findings are summarized as follows.

1. The ALMA observations of the [C II] line emission from this quasar resulted in a systemic redshift calculation of $z = 5.832 \pm 0.001$. We find a [C II] line width of 440 ± 80 km s^{-1}. The [C II] luminosity is $1.23 \times 10^9\ L_\odot$, comparable to values reported in other high-redshift quasars in the

literature. The derived SFR from the [C II] emission is $SFR_{[C\,II]} = 54–285\ M_\odot\ yr^{-1}$. Finally, the ALMA observations revealed an underlying unresolved continuum source at 290 GHz with a flux density of 0.34 ± 0.04 mJy (see Figures 1–3).

2. We do not detect the CO (6–5) emission line in our NOEMA 100 GHz observation. The derived 3σ upper limit is <0.35 mJy, corresponding to a luminosity $L_{CO\ (6-5)} < 0.5 \times 10^9\ L_\odot$ (assuming the same FWHM as measured for the [C II] line). Continuum emission is detected with NOEMA at 100 GHz with a flux density of 0.10 ± 0.01 mJy (see Figure 3).
3. The high-S/N GMRT 215 MHz observations of the quasar allow us to improve the constraints on the radio emission at low frequencies (see Bañados et al. 2018). The synchrotron radiation can be well modeled by a simple power law with spectral index $\alpha_3^{0.215} = -0.88 \pm 0.08$. This resulted in updating the calculation of the quasar's radio-loudness parameter $R_{4400} = 1100 \pm 280$ and $R_{2500} = 1470^{+110}_{-100}$, confirming its prominent radio power (see Figure 4).
4. We study the dust emission of the quasar host galaxy by using the typical approach of modeling a modified MBB to our two millimeter-continuum measurements from ALMA 290 GHz and NOEMA 100 GHz. However, the NOEMA measurement is an order of magnitude brighter than expected from the MBB scaled to the ALMA emission using the typical $T_{dust} = 47$ K and $\beta = 1.6$ and cannot be modeled by any other dust parameters commonly used in the literature. Therefore, we hypothesize that the 100 GHz continuum emission is dominated by synchrotron radiation. However, the emission is three times dimmer than the expected emission by extrapolating the trend at lower frequencies. This implies a break in the synchrotron spectrum (see Figure 4).
5. From the ALMA 290 GHz continuum observations we derive the FIR properties of the quasar, assuming that this data point is not significantly contaminated by synchrotron emission (see discussion in Section 5.1). Assuming an MBB with typical parameters ($T_{dust} = 47$ K and $\beta = 1.6$), we derive a dust mass and FIR and TIR luminosities. These quantities are reported in Table 3. The SFR derived from the L_{TIR} is $SFR_{TIR} = 110.0 \pm 13.0\ M_\odot\ yr^{-1}$, which is consistent with the calculated SFR from the [C II] emission.
6. This quasar lies within typical estimates of [C II] FWHM, $EW_{[C\,II]}$, $L_{[C\,II]}$, and L_{FIR} compared to quasars at $z \gtrsim 6$ in the literature. We highlight that the derived properties of P352–15 are very similar to quasar J2318–3113, which is the only other radio-loud quasar with [C II] and rest-frame FIR studies (see Figure 5). A more comprehensive study of high-redshift radio quasars in the millimeter is required for statistical comparisons.

The extreme radio brightness of the quasar P352–15 makes it an ideal laboratory to study the effects of powerful radio jets on the formation of SMBHs and galaxies during the first gigayear of cosmic time. This quasar presents an intriguing SED (Figure 4) and leaves more open questions that make it an excellent target for follow-up observations. For example, to evaluate the turnover frequency of the synchrotron spectrum, observations filling the gap between the existing 3 and 100 GHz measurements are required (as shown in Figure 4). If the slope steepens at observed frequencies higher than 3 GHz, we can assume that the ALMA observations sample the dust emission while the NOEMA emission is dominated by synchrotron. This way it would be possible to disentangle the synchrotron from dust emission. Furthermore, at these high frequencies the relativistic electrons dissipate much faster, assuming that synchrotron radiation is the main dissipation mechanism, causing a steepening of the synchrotron spectrum (Scheuer & Williams 1968; Pacholczyk 1970; Condon & Ransom 2016). Therefore, by identifying the turnover frequency, we would be able to gauge the age of the radio jet (e.g., Myers & Spangler 1985; Carilli et al. 1991). Finally, our current data marginally resolve the [C II] emission (Figure 1); higher-resolution observations could reveal potential signatures of ongoing merger or outflow in this quasar. All of these open questions can be addressed with future observations from existing facilities such as ALMA, NOEMA, and the VLA.

We thank Charlène Lefèvre at IRAM for the great help and guidance reducing the NOEMA data used in this work. S.R.R. acknowledges financial support from the International Max Planck Research School for Astronomy and Cosmic Physics at the University of Heidelberg (IMPRS–HD). The work of T.C. was carried out at the Jet Propulsion Laboratory, California Institute of Technology, under a contract with NASA. A.C.E. acknowledges support by NASA through the NASA Hubble Fellowship grant No. HF2-51434 awarded by the Space Telescope Science Institute, which is operated by the Association of Universities for Research in Astronomy, Inc., for NASA, under contract NAS5-26555. The National Radio Astronomy Observatory is a facility of the National Science Foundation operated under cooperative agreement by Associated Universities, Inc.

This paper makes use of ALMA data in program ADS/JAO. ALMA# 2019.1.00840.S. The Joint ALMA Observatory is operated by ESO, AUI/NRAO and NAOJ. This work is based on observations carried out under project No. W18EG with the IRAM NOEMA Interferometer. IRAM is supported by INSU/CNRS (France), MPG (Germany), and IGN (Spain). This paper uses GMRT observations from program ddtC007. We thank the staff of the GMRT that made these observations possible. GMRT is run by the National Centre for Radio Astrophysics of the Tata Institute of Fundamental Research.

Facilities: ALMA, IRAM:NOEMA, GMRT.

Software: Astropy (The Astropy Collaboration et al. 2013), CASA (McMullin et al. 2007), Interferopy (https://github.com/mladenovak/interferopy), Matplotlib (Hunter 2007), Numpy (Harris et al. 2020).

ORCID iDs

Sofía Rojas-Ruiz https://orcid.org/0000-0003-2349-9310
Eduardo Bañados https://orcid.org/0000-0002-2931-7824
Marcel Neeleman https://orcid.org/0000-0002-9838-8191
Thomas Connor https://orcid.org/0000-0002-7898-7664
Anna-Christina Eilers https://orcid.org/0000-0003-2895-6218
Bram P. Venemans https://orcid.org/0000-0001-9024-8322
Yana Khusanova https://orcid.org/0000-0002-7220-397X
Chris Carilli https://orcid.org/0000-0001-6647-3861
Chiara Mazzucchelli https://orcid.org/0000-0002-5941-5214
Roberto Decarli https://orcid.org/0000-0002-2662-8803
Emmanuel Momjian https://orcid.org/0000-0003-3168-5922
Mladen Novak https://orcid.org/0000-0001-8695-825X

References

Astropy Collaboration, Robitaille, T. P., Tollerud, E. J., et al. 2013, A&A, 558, A33
Bañados, E., Carilli, C., Walter, F., et al. 2018, ApJL, 861, L14
Bañados, E., Decarli, R., Walter, F., et al. 2015a, ApJL, 805, L8
Bañados, E., Mazzucchelli, C., Momjian, E., et al. 2021, ApJ, 909, 80
Bañados, E., Venemans, B. P., Decarli, R., et al. 2016, ApJS, 227, 11
Bañados, E., Venemans, B. P., Morganson, E., et al. 2015b, ApJ, 804, 118
Beelen, A., Cox, P., Benford, D. J., et al. 2006, ApJ, 642, 694
Belladitta, S., Moretti, A., Caccianiga, A., et al. 2019, A&A, 629, A68
Belladitta, S., Moretti, A., Caccianiga, A., et al. 2020, A&A, 635, L7
Bischetti, M., Maiolino, R., Carniani, S., et al. 2019, A&A, 630, A59
Briggs, D. S., Schwab, F. R., & Sramek, R. A. 1999, ASPC, 180, 127
Carilli, C., & Walter, F. 2013, ARA&A, 51, 105
Carilli, C. L., Perley, R. A., Dreher, J. W., & Leahy, J. P. 1991, ApJ, 383, 554
Chabrier, G. 2003, PASP, 115, 763
Condon, J. J., & Ransom, S. M. 2016, Essential Radio Astronomy (Princeton, NJ: Princeton Univ. Press)
Connor, T., Bañados, E., Stern, D., et al. 2021, ApJ, 911, 120
da Cunha, E., Groves, B., Walter, F., et al. 2013, ApJ, 766, 13
de Gasperin, F., Intema, H. T., & Frail, D. A. 2018, MNRAS, 474, 5008
De Looze, I., Cormier, D., Lebouteiller, V., et al. 2014, A&A, 568, A62
Decarli, R., Walter, F., Venemans, B. P., et al. 2018, ApJ, 854, 97
Decarli, R., Walter, F., Yang, Y., et al. 2012, ApJ, 756, 150
Díaz-Santos, T., Armus, L., Charmandaris, V., et al. 2017, ApJ, 846, 32
Dunne, L., Eales, S., Edmunds, M., et al. 2000, MNRAS, 315, 115
Dunne, L., Eales, S. A., & Edmunds, M. G. 2003, MNRAS, 341, 589
Duric, N., Bourneuf, E., & Gregory, P. C. 1988, AJ, 96, 81
Eilers, A. C., Hennawi, J. F., Decarli, R., et al. 2020, ApJ, 900, 37
Eilers, A. C., Hennawi, J. F., Decarli, R., et al. 2021, ApJ, 914, 74
Farrah, D., Lebouteiller, V., Spoon, H. W. W., et al. 2013, ApJ, 776, 38
Ghisellini, G., Tagliaferri, G., Sbarrato, T., & Gehrels, N. 2015, MNRASL, 450, L34
Ghisellini, G., Tavecchio, F., Foschini, L., et al. 2010, MNRAS, 402, 497
Harris, C. R., Millman, K. J., van der Walt, S. J., et al. 2020, Natur, 585, 357
Hunter, J. D. 2007, CSE, 9, 90
Hurley-Walker, N., Callingham, J. R., Hancock, P. J., et al. 2017, MNRAS, 464, 1146
Ighina, L., Belladitta, S., Caccianiga, A., et al. 2021, A&A, 647, L11
Ighina, L., Caccianiga, A., Moretti, A., et al. 2019, MNRAS, 489, 2732
Inayoshi, K., Visbal, E., & Haiman, Z. 2020, ARA&A, 58, 27
Intema, H. T., Jagannathan, P., Mooley, K. P., & Frail, D. A. 2017, A&A, 598, A78
Izumi, T., Onoue, M., Shirakata, H., et al. 2018, PASJ, 70, 36
James, A., Dunne, L., Eales, S., & Edmunds, M. G. 2002, MNRAS, 335, 753
Jolley, E. J. D., & Kuncic, Z. 2008, MNRAS, 386, 989
Kaviraj, S., Laigle, C., Kimm, T., et al. 2017, MNRAS, 467, 4739
Kellermann, K. I., Sramek, R., Schmidt, M., Shaffer, D. B., & Green, R. 1989, AJ, 98, 1195
Kennicutt, R. C. 1998, ARA&A, 36, 189
Kennicutt, R. C., & Evans, N. J. 2012, ARA&A, 50, 531
Kormendy, J., & Ho, L. C. 2013, ARA&A, 51, 511
Leipski, C., Meisenheimer, K., Walter, F., et al. 2014, ApJ, 785, 154
Liu, Y., Wang, R., Momjian, E., et al. 2021, ApJ, 908, 124
Malhotra, S., Kaufman, M. J., Hollenbach, D., et al. 2001, ApJ, 561, 766
Marshall, M. A., Mechtley, M., Windhorst, R. A., et al. 2020, ApJ, 900, 21
Mazzucchelli, C., Bañados, E., Venemans, B. P., et al. 2017, ApJ, 849, 91
McMullin, J. P., Waters, B., Schiebel, D., Young, W., & Golap, K. 2007, in ASP Conf. Ser. 376, Astronomical Data Analysis Software and Systems XVI, ed. R. A. Shaw, F. Hill, & D. J. Bell (San Francisco, CA: ASP), 127
Mechtley, M., Windhorst, R. A., Ryan, R. E., et al. 2012, ApJL, 756, L38
Momjian, E., Carilli, C. L., Bañados, E., Walter, F., & Venemans, B. P. 2018, ApJ, 861, 86
Myers, S. T., & Spangler, S. R. 1985, ApJ, 291, 52
Nanni, R., Gilli, R., Vignali, C., et al. 2018, A&A, 614, A121
Neeleman, M., Novak, M., Venemans, B. P., et al. 2021, ApJ, 911, 141
Novak, M., Bañados, E., Decarli, R., et al. 2019, ApJ, 881, 63
Novak, M., Venemans, B. P., Walter, F., et al. 2020, ApJ, 904, 131
Pacholczyk, A. G. 1970, Series of Books in Astronomy and Astrophysics (San Francisco: Freeman)
Perley, R. A., & Butler, B. J. 2017, ApJS, 230, 7
Priddey, R. S., & McMahon, R. G. 2001, MNRAS, 324, L17
Regan, J. A., Downes, T. P., Volonteri, M., et al. 2019, MNRAS, 486, 3892
Romani, R. W., Sowards-Emmerd, D., Greenhill, L., & Michelson, P. 2004, ApJL, 610, L9
Salpeter, E. E. 1955, ApJ, 121, 161
Sargsyan, L., Samsonyan, A., Lebouteiller, V., et al. 2014, ApJ, 790, 15
Sbarrato, T., Ghisellini, G., Nardini, M., et al. 2012, MNRAS, 426, L91
Scheuer, P. A. G., & Williams, P. J. S. 1968, ARA&A, 6, 321
Schöier, F. L., van der Tak, F. F. S., van Dishoeck, E. F., & Black, J. H. 2005, A&A, 432, 369
Shao, Y., Wang, R., Carilli, C. L., et al. 2019, ApJ, 876, 99
Sramek, R. A., & Weedman, D. W. 1980, ApJ, 238, 435
Taylor, E. N., Hopkins, A. M., Baldry, I. K., et al. 2011, MNRAS, 418, 1587
Venemans, B. P., Decarli, R., Walter, F., et al. 2018, ApJ, 866, 159
Venemans, B. P., McMahon, R. G., Walter, F., et al. 2012, ApJL, 751, L25
Venemans, B. P., Walter, F., Decarli, R., et al. 2017a, ApJ, 845, 154
Venemans, B. P., Walter, F., Decarli, R., et al. 2017b, ApJL, 851, L8
Venemans, B. P., Walter, F., Neeleman, M., et al. 2020, ApJ, 904, 130
Venemans, B. P., Walter, F., Zschaechner, L., et al. 2016, ApJ, 816, 37
Volonteri, M., Silk, J., & Dubus, G. 2015, ApJ, 804, 148
Wang, F., Yang, J., Fan, X., et al. 2019, ApJ, 884, 30
Wang, R., Wagg, J., Carilli, C. L., et al. 2013, ApJ, 773, 44
Weiß, A., Kovács, A., Güsten, R., et al. 2008, A&A, 490, 77
Willott, C. J., Bergeron, J., & Omont, A. 2015, ApJ, 801, 123
Yun, M. S., & Carilli, C. L. 2002, ApJ, 568, 88
Zibetti, S., Charlot, S., & Rix, H.-W. 2009, MNRAS, 400, 1181